PHYSICAL REVIEW E **103**, 033001 (2021)

Volume-constrained deformation of a thin sheet as a route to harvest elastic energy

Oz Oshri[*]

Department of Mechanical Engineering, Ben-Gurion University of the Negev, Beer-Sheva 84105, Israel

(Received 8 November 2020; revised 2 February 2021; accepted 8 February 2021; published 2 March 2021)

Thin sheets exhibit rich morphological structures when subjected to external constraints. These structures store elastic energy that can be released on demand when one of the constraints is suddenly removed. Therefore, when adequately controlled, shape changes in thin bodies can be utilized to harvest elastic energy. In this paper, we propose a mechanical setup that converts the deformation of the thin body into a hydrodynamic pressure that potentially can induce a flow. We consider a closed chamber that is filled with an incompressible fluid and is partitioned symmetrically by a long and thin sheet. Then, we allow the fluid to exchange freely between the two parts of the chamber, such that its total volume is conserved. We characterize the slow, quasistatic, evolution of the sheet under this exchange of fluid, and derive an analytical model that predicts the subsequent pressure drop in the chamber. We show that this evolution is governed by two different branches of solutions. In the limit of a small lateral confinement we obtain approximated solutions for the two branches and characterize the transition between them. Notably, the transition occurs when the pressure drop in the chamber is maximized. Furthermore, we solve our model numerically and show that this maximum pressure behaves nonmonotonically as a function of the lateral compression.

DOI: 10.1103/PhysRevE.103.033001

I. INTRODUCTION

Thin sheets are pliable solid objects that can undergo pronounced morphological transitions when they are constrained by external forces or internal geometric frustrations [1–19]. These morphological transitions release elastic energy that, if properly managed, can be exploited for the purpose of energy harvesting; see recent reviews on the subject in Refs. [20–29] and references therein.

Herein, we study a mechanical system that converts the elastic energy stored in a thin sheet, into a hydrodynamic pressure that potentially can enable a flow. Our system consists of an inextensible sheet that is laterally confined between the two sides of a rectangular closed chamber (Fig. 1). Had we kept the system in this configuration the sheet would buckle to accommodate the external compression, which is manifested by the first mode of buckling in the framework of Euler's elastica [30,31]. However, we further fill the chamber with an incompressible fluid that fixes the volumes above and below the sheet. This additional confinement requires the sheet to accommodate a configuration that is higher in energy compared with the trivial first mode of buckling. Then, we connect the two sides of the chamber and allow an exchange of fluid between them, i.e., essentially we remove the second confinement while keeping the lateral compression fixed. The system now becomes unstable because the sheet can spontaneously lower its bending energy by a proper transfer of fluid between the two sides of the chamber. Therefore, the energetic gap between the initial and final configurations is utilized to create a pressure drop, and consequently a flow.

Patterns' transitions in thin sheets that are confined in parallel by two or more constraints have been the subject of several recent studies, either for the purpose of a fundamental research or for practical usage in technological applications [32–36]. In many cases, when one of the constraints is modified, or even completely removed, the system spontaneously jumps between two of its equilibrium configurations. For example, a thin arch that is uniaxially compressed from the boundaries, and at the same time subjected to a concentrated force at its midpoint, is known to undergo a rapid transition to an inverted shape when the force exceeds a threshold value [37,38].

This rapid transition between two possible solutions of the equilibrium equations is called the "snap-through" instability and is discussed in detail in Refs. [38–47].

Similar to the aforementioned studies, the thin sheet in our system is expected to change its orientation rapidly when the constraint over the volume is removed. While this rapid transition can lead to a complex, time-dependent, behavior of both the sheet and the fluid, as a first step of studying the system we will neglect inertial effects and focus on its quasistatic evolution. Under this limiting assumption we derive an analytical model that predicts the elastic configuration of the sheet as a function of the volume difference in the chamber.

Although our model yields a set of nonlinear differential equations, in the limit of a small lateral confinement we obtain exact and tractable solutions that shed light on the evolution of the system. Similar to the analysis in Refs. [38,48] we find that the system evolves in between two limiting configurations that belong to two different branches of solutions. One is an "asymmetric branch" that converges to the second, asymmetric mode of buckling when the volume difference between the two sides of the chamber vanishes and second is a "symmetric

---

[*] oshrioz@bgu.ac.il

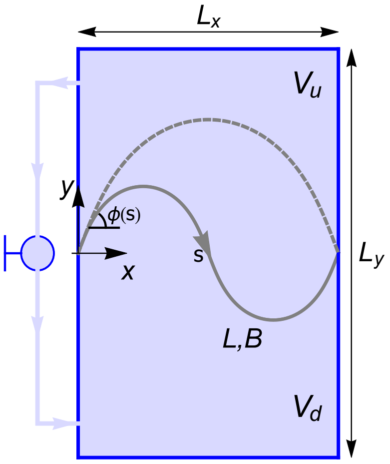

FIG. 1. Schematic overview of the system. Thin sheet with total length L and bending modulus B is compressed symmetrically between the two sides of a rectangular closed chamber. The dimensions of the chamber are $L_x \times L_y$. A Cartesian coordinate system is located on the left edge of the sheet at a height $L_y/2$ above the bottom wall. In the initial setup the valve is closed and the two sides of the chamber are filled with an incompressible fluid with equal volumes, $V_\mathrm{u} = V_\mathrm{d}$. Under this setup the sheet accommodates an elastic shape (solid-gray line) that is higher in energy compared with the first mode of buckling (dashed-gray line). Then we open the valve and allow a controllable exchange of fluid between the two sides of the chamber. The sheet now spontaneously relaxes its bending energy until it reaches the lower energetic state.

branch" that converges to the first, symmetric mode of buckling when the volume difference reaches a maximum value. During this evolution from the second to the first modes of buckling, the pressure difference between the two sides of the chamber increases from zero to some maximum value and than decreases back to zero. Notably, we show that this pressure difference is maximized at the critical point where the asymmetric-to-symmetric transition occurs. We further investigate the solution of our model numerically, beyond the small amplitude approximation, and show that under some predesigned conditions the maximum pressure behaves nonmonotonically as a function of the lateral compression.

The paper is organized as follows. In Sec. II we formulate the problem and derive a closed set of differential equations that determines the sheet's configuration at a given volume difference. In Sec. III we derive an approximated solution to the asymmetric and the symmetric branches in the limit of a small lateral confinement and analyze the transition between them. In Sec. IV we solve our model numerically beyond the small amplitude approximation and discuss the effect of the lateral compression on the maximum pressure drop in the chamber. In Sec. V we conclude and discuss possible extensions for future studies.

II. FORMULATION OF THE PROBLEM

An inextensible thin sheet with bending modulus B, thickness t, and total length L is confined between the two sides of a rectangular closed chamber, see Fig. 1. The horizontal, the vertical, and the width dimensions of the chamber are denoted by L_x ($L \geqslant L_x$), L_y, and W, respectively. The two sides of the chamber, above and below the elastic sheet, are filled with an incompressible fluid with volumes V_u and V_d, respectively.

Initially, we set $V_\mathrm{u} = V_\mathrm{d}$. Then we connect the two sides of the chamber and allow a controllable exchange of fluid between them, see Fig. 1. Since under this initial setup the elastic configuration does not accommodate its lowest energetic state, we would expect it to snap and enhance the fluid exchange. While this change in the sheet's configuration can result in a rapid and irreversible flow, in this work we neglect dynamic effects and focus on the slow, quasistatic, evolution of the system. The amount of fluid transferred between the two sides of the chamber is our control parameter. An alternative scenario in which the pressure difference in the chamber is the control parameter is discussed in Appendix A.

Additionally, we place the following three assumptions. First, we assume that no contact occurs between the sheet and the side walls of the chamber and no self-contact occurs in the sheet. Second, we assume that the system remains invariant along the W direction, and therefore, without loss of generality set $W = 1$. Third, we assume that the volume occupied by the elastic sheet is negligible compared with the total volume of the chamber, i.e., $tL/L_xL_y \ll 1$, and as a result $V_\mathrm{u} + V_\mathrm{d} = L_xL_y$.

To characterize the elastic configuration on the xy plane we place a Cartesian coordinate system on the left edge of the sheet, $0 \leqslant x \leqslant L_x$ and $-L_y/2 \leqslant y \leqslant L_y/2$, and define the angle $\phi(s)$ between the tangent to sheet and the x axis. With these definitions the position vector $\mathbf{x}(s) = [x(s), y(s)]$ is given by

$$x(s) = \int_0^s \cos\phi(s')ds', \tag{1a}$$

$$y(s) = \int_0^s \sin\phi(s')ds', \tag{1b}$$

where $s \in [0, L]$ is the arclength parameter.

Given the total volume of the chamber L_xL_y and the amount of fluid filling the bottom part V_d, we look for the elastic configuration that minimizes the following energy:

$$E = \frac{B}{2}\int_0^L \dot{\phi}^2 ds, \tag{2}$$

where $(\dot{\ }) = d/ds$. This energy, which accounts for the bending deformation of the sheet, must be minimized under three constraints; two that account for the geometric relations, Eqs. (1), and one that accounts for the volumes of the fluid above and below the elastic sheet. Using Green's theorem we can relate the latter volumes to the sheet's configuration by

$$V_\mathrm{i} = \frac{1}{2}\int_0^L \mathbf{x}\cdot\hat{\mathbf{n}}_\mathrm{i} ds + \frac{L_xL_y}{2}, \tag{3}$$

where $i = u, d$ and $\hat{\mathbf{n}}_\mathrm{i} = \pm(-\sin\phi, \cos\phi)$ is the outward normal vector to the enclosed area.

To obtain the equilibrium equations we first normalize the energy by B/L, and all lengths by the total length of the sheet L, say $s \to s/L$ such that $s \in [0, 1]$. Second, we modify the energy, Eq. (2), to account for the various constraints

$$\mathcal{G} = \int_0^1 \left[\frac{1}{2}\dot{\phi}^2 - Q_x(s)(\dot{x} - \cos\phi) - Q_y(s)(\dot{y} - \sin\phi)\right] ds + P_{\mathrm{ud}}\left(\frac{1}{2}\int_0^1 \mathbf{x}\cdot\hat{\mathbf{n}}_{\mathrm{d}} ds + \frac{L_y}{2} - V_d\right), \tag{4}$$

where $Q_x(s)$ and $Q_y(s)$ are two Lagrange multipliers that account, respectively, for the two geometric constraints, Eqs. (1), and P_{ud} is a Lagrange multiplier that accounts for the constraint over the fluid's volumes, Eq. (3). As a result, $P_{\mathrm{ud}} = P_{\mathrm{u}} - P_{\mathrm{d}}$ is the normalized pressure drop between the two sides of the chamber ($P_{\mathrm{ud}} \to P_{\mathrm{ud}}L^3/B$); P_{u} and P_{d} denote, respectively, the normalized pressures above and below the sheet. Note that, since we are considering the quasistatic evolution of the system, these pressures remain constant in each side of the chamber for a given volume difference.

Third, we minimize the total energy, Eq. (4), with respect to $\{\phi(s), x(s), y(s), Q_x(s), Q_y(s)\}$. This minimization yields the following equilibrium equations:

$$\ddot{\phi} + \frac{P_{\mathrm{ud}}}{2}(x\cos\phi + y\sin\phi) + Q_x\sin\phi - Q_y\cos\phi = 0, \tag{5a}$$

$$\dot{x} - \cos\phi = 0, \tag{5b}$$

$$\dot{y} - \sin\phi = 0, \tag{5c}$$

$$\dot{Q}_x - \frac{P_{\mathrm{ud}}}{2}\sin\phi = 0, \tag{5d}$$

$$\dot{Q}_y + \frac{P_{\mathrm{ud}}}{2}\cos\phi = 0. \tag{5e}$$

Keeping in mind the order of these equations, and that P_{ud} is yet an unknown constant, we obtain a closure once we add the following boundary conditions:

$$x(0) = 0, \tag{6a}$$

$$x(1) = L_x \equiv 1 - \Delta, \tag{6b}$$

$$y(0) = y(1) = 0, \tag{6c}$$

$$\dot{\phi}(0) = \dot{\phi}(1) = 0, \tag{6d}$$

where in Eq. (6b) we defined the lateral compression $\Delta \equiv 1 - L_x$, and we specialized to sheets that are hinged to the side walls of the chamber, Eq. (6d). In addition, instead of accounting separately for the volume of the fluid below or above the elastic sheet, as given by Eq. (3), we will account for the volume difference

$$V_{\mathrm{du}} \equiv V_{\mathrm{d}} - V_{\mathrm{u}} = \int_0^1 \mathbf{x}\cdot\hat{\mathbf{n}}_{\mathrm{d}} ds. \tag{7}$$

Given V_{du} we can determine the volume in each side of the chamber from Eq. (3). In the following analysis we always assume that the sheet buckles upward, i.e., $V_{\mathrm{du}} > 0$ and fluid is transferred from the upper side of the chamber to the lower side such that the pressure drop $P_{\mathrm{ud}} > 0$ remains positive. We keep in mind that the system has a mirror symmetry around the x axis, and therefore a deformation in the opposite direction, i.e., downward with $V_{\mathrm{du}} < 0$ and $P_{\mathrm{ud}} < 0$, would yield the reflection of the former upward solution.

Although Eqs. (5) to (7) form closure, they can further be simplified using direct integration of Eqs. (5d) and (5e). Indeed, utilizing the geometric constraints, Eqs. (5b) and (5c), we obtain, $Q_x(s) = P_{\mathrm{ud}}y/2 + P_x$ and $Q_y(s) = -P_{\mathrm{ud}}x/2 + P_y$. Substituting the latter expressions in Eq. (5a) gives

$$\ddot{\phi} + P_{\mathrm{ud}}(x\cos\phi + y\sin\phi) + P_x\sin\phi - P_y\cos\phi = 0. \tag{8}$$

Equation (8) describes the balance of normal forces on a finite element of the sheet. Within this balance of forces the constants P_x and P_y denote the normalized reaction forces ($P_x \to P_xL^2/B$) in the x and y directions that the chamber applies on the sheet at $s = 0$. We note that Eq. (8) can further be reduced into a canonical form from which an exact solution in terms of the Jacobi elliptic functions can be derived [49]. For completeness, this solution is provided in Appendix B. Nonetheless, in the present paper we will not make direct use of this exact solution because it further requires the numerical solution of transcendental equations that are related to the boundary conditions [50,51]. The complexity of solving these transcendental equations is similar to that of finding the numerical solution of Eq. (8).

This completes the formulation of the problem. In summary, given the difference in volume between the upper and lower sides of the chamber V_{du} and the lateral compression Δ, we can solve Eqs. (5) to (7) to obtain the spatial configuration $\mathbf{x}(s)$ and the pressure drop P_{ud}. Alternatively, solving Eqs. (5b), (5c), and (8), together with the boundary conditions, Eqs. (6) and (7) yield the same solution.

Schematic evolution of the system

Before we proceed to derive an approximated analytical solution to the system, we schematically describe its evolution. Our initial setup requires the volume difference in the chamber to vanish $V_{\mathrm{du}} = 0$. One possible configuration that naturally complies with this requirement is an asymmetric shape of the elastic sheet. Not only does an asymmetric shape satisfies $V_{\mathrm{u}} = V_{\mathrm{d}}$, it also implies that $P_{\mathrm{ud}} = 0$. This is because of the up-down symmetry that this configuration acquires. When the pressure drop vanishes in the chamber Eq. (8) coincides with the theory of Euler's elastica [52,53], which describes the deformation a laterally compressed rod. Since, in that theory the second mode of buckling has the lowest energy among all other asymmetric solutions, it is the one that is expected to appear in our system.

As long as no fluid is allowed to transfer between the two sides of the chamber the asymmetric shape remains stable. It becomes unstable once the two sides of the chamber are connected. This is because the sheet can then spontaneously relax its bending energy and thereby lower the total elastic energy of the system. This spontaneous relaxation increases the pressure drop in the chamber and essentially promotes the fluid exchange. This process continues to occur until P_{ud} vanishes altogether, or equivalently until the sheet accommodates its lowest energetic state. This state is again a solution to Euler's elastica because $P_{\mathrm{ud}} = 0$ and corresponds to the first (symmetric) mode of buckling in this theory. Of course, we keep in mind that our system behaves quasistatically, and therefore the exchange of fluid is considered in a controllable manner.

Consequently, the system is expected to evolve in between two limiting configurations. The first limiting configuration corresponds to the second (asymmetric) mode of buckling

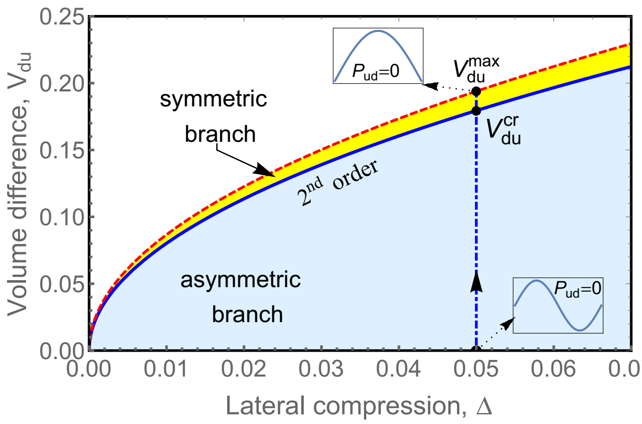

FIG. 2. Schematic phase diagram on the $(\Delta, V_{\rm du})$ plane. As the volume difference increases continuously from zero the system evolves in between two different branches of solutions. While the asymmetric branch dominates the system between $0 < V_{\rm du} < V_{\rm du}^{\rm cr}$ (light-blue shaded area) the symmetric branch dominates between $V_{\rm du}^{\rm cr} < V_{\rm du} < V_{\rm du}^{\rm max}$ (yellow-shaded area). The critical and maximum volume differences, $V_{\rm du}^{\rm cr}$ and $V_{\rm du}^{\rm max}$, are denoted by the solid blue and red-dashed lines, respectively. In the small amplitude approximation $V_{\rm du}^{\rm cr}$ is given by Eq. (13b) and $V_{\rm du}^{\rm max} = \frac{8}{\pi^2}\Delta^{1/2}$. The asymmetric-to-symmetric transition is always of a second order. While at $V_{\rm du} = 0$ the system converges to the first limiting solution, i.e., the asymmetric mode with $P_{\rm ud} = 0$, at $V_{\rm du} = V_{\rm du}^{\rm max}$ the system converges to the symmetric mode of buckling that satisfies again $P_{\rm ud} = 0$. Increasing the volume difference beyond $V_{\rm du}^{\rm max}$ requires that $P_{\rm ud} < 0$, and therefore is beyond the scope of our investigation.

within the theory of Euler's elastica, which satisfies $V_{\rm du} = 0$ and $P_{\rm ud} = 0$. The second limiting configuration corresponds to the first (symmetric) mode of buckling within that theory. This symmetric configuration corresponds to the maximum volume difference that the system can spontaneously acquire $V_{\rm du} = V_{\rm du}^{\rm max}$ and satisfies again $P_{\rm ud} = 0$. In the following analysis we will show that these two limiting configurations originate from different branches of solutions that we will call the "asymmetric" branch and the "symmetric" branch. As a result, the evolution of the system includes a nontrivial asymmetric-to-symmetric transition. Our analysis will focus on the derivation of these two branches and the critical conditions at which the transition occurs. To remind the reader of the different regions of the system, we point to the "phase-diagram" in Fig. 2, where the stability regions of these branches are plotted schematically on the $(\Delta, V_{\rm du})$ plane. We note that this schematic description is similar to that of the force-displacement relation in Ref. [48], where the pressure difference and the volume difference take, respectively, the roles of the concentrated force applied on the midpoint of the beam and its corresponding vertical displacement.

III. APPROXIMATED SOLUTION IN THE LIMIT $\Delta \ll 1$ FOR HINGED SHEETS

In this section we derive an approximated solution to the problem under the assumption that the lateral compression $\Delta \equiv 1 - L_x$ remains small. This assumption allows us to expand the equilibrium equations to leading order in powers of the profile's amplitude $y(s)$. Within this expansion, the geometric constraints, Eqs. (5b) and (5c), reduce to $x(s) \simeq s - \frac{1}{2}\int_0^s \phi(s)^2 ds$ and $\dot{y}(s) \simeq \phi(s)$. Substituting these expressions in Eq. (8) and linearizing gives

$$\dddot{y} + P_x \dot{y} = -P_{\rm ud} s + P_y. \tag{9}$$

The solution of this linear equation is given by

$$y(s) = a_1 + a_2 \cos(\sqrt{P_x} s) + a_3 \sin(\sqrt{P_x} s) + \frac{P_y}{P_x} s - \frac{P_{\rm ud}}{2P_x} s^2, \tag{10}$$

where a_i $(i = 1 \dots 3)$, P_x, P_y, and $P_{\rm ud}$ are six unknown constants that are yet to be determined by the boundary conditions, Eqs. (6b) to (6d), and the constraint over the volumes Eq. (7). Note that in this leading-order approximation the lateral compression of the sheet Eq. (6b) is approximated by $\Delta = \frac{1}{2}\int_0^1 \dot{y}^2 ds$, and the volume difference Eq. (7) reduces to $V_{\rm du} = 2\int_0^1 y(s) ds$.

Let us characterize now the evolution of the system from the asymmetric branch to the symmetric branch. In the following three sections we first derive the solutions for these branches and then analyze the transition between them.

A. Asymmetric branch

To derive the asymmetric branch we first fix the lateral compression at a constant value $P_x = 4\pi^2$. Then we utilize the boundary conditions Eqs. (6) and the linearized solution Eq. (10) to obtain the height profile. The solution reads

$$\begin{aligned} y(s) = {} & \frac{P_{\rm ud}}{16\pi^4}[2\pi^2(1 - s)s + 1 - \cos(2\pi s)] \\ & + \frac{1}{\pi}\sqrt{\Delta - \frac{15 + 2\pi^2}{768\pi^6} P_{\rm ud}^2} \sin(2\pi s). \end{aligned} \tag{11}$$

Note that when $P_{\rm ud} \to 0$ this configuration converges to $y(s) \to \sqrt{\Delta/\pi^2}\sin(2\pi s)$, as expected from the second mode of buckling in the theory of Euler's elastica and in the respected limit of the small amplitude approximation. To complete the solution we also need to find the relation between the volume difference $V_{\rm du}$ and the pressure drop $P_{\rm ud}$. Using the linearized form of Eq. (7) we obtain

$$V_{\rm du} = \frac{3 + \pi^2}{24\pi^4} P_{\rm ud}. \tag{12}$$

Therefore, in the small amplitude approximation the $P_{\rm ud}$-$V_{\rm du}$ relation of the asymmetric branch is linear and independent of Δ. Equations (11) and (12) essentially provide the complete solution of the asymmetric branch.

Evidently, for a given lateral compression Δ the asymmetric branch ceases to exist when the term under the square-root in Eq. (11) becomes negative. This happens at the critical pressure and volume difference

$$P_{\rm ud}^{\rm cr} = \sqrt{\frac{768\pi^6}{15 + 2\pi^2}} \Delta^{1/2}, \tag{13a}$$

$$V_{\rm du}^{\rm cr} = \frac{2(3 + \pi^2)}{\pi\sqrt{3(15 + 2\pi^2)}} \Delta^{1/2}. \tag{13b}$$

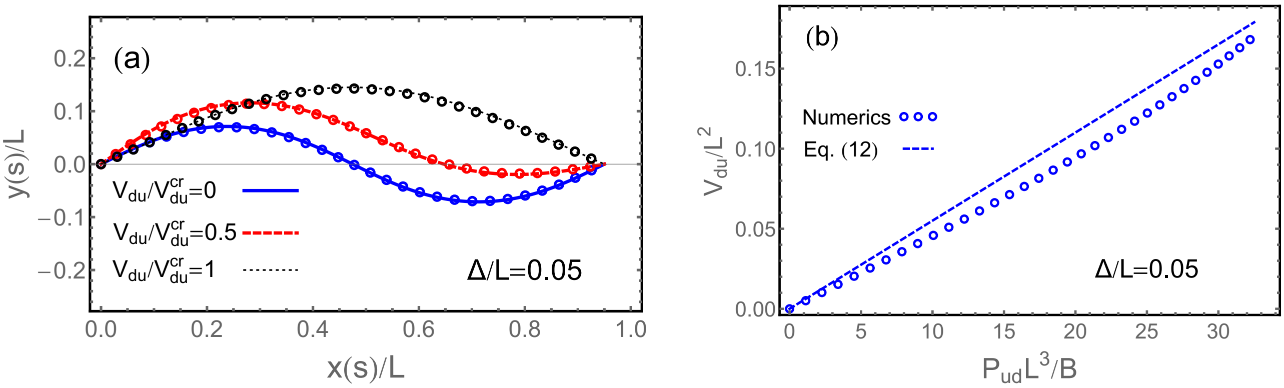

FIG. 3. The evolution of the asymmetric branch when $\Delta/L = 0.05$. The explicit normalization is presented in the axes of both panels. (a) The spatial configuration of the sheet for several values of V_{du}/V_{du}^{cr}. The critical volume difference is given numerically by $V_{du}^{cr}/L^2 \simeq 0.169$ and analytically by $V_{du}^{cr}/L^2 \simeq 0.179$, see Eq. (13b). Note that the comparisons between the analytical and numerical solutions are presented for the relative volume difference, V_{du}/V_{du}^{cr}, and not for the absolute value of V_{du}/L^2. While open circles correspond to the numerical solution of Eqs. (5b), (5c), and (8), blue solid, red dashed, and black dotted lines correspond to the approximated analytical solution, Eqs. (11), (12), and $x(s) = s - \frac{1}{2}\int_0^s \dot{y}(s')^2 ds'$. When $V_{du}/V_{du}^{cr} = 0$ the elastic configuration converges to the second (asymmetric) mode of buckling within the theory of Euler's elastica. (b) The volume difference is plotted as a function of the pressure drop, where the blue dashed line corresponds to the analytical prediction, Eq. (12), and open circles to the numerical solution.

In Sec. III C we will show that these critical values coincide with the critical point at which the asymmetric-to-symmetric transition occurs.

This completes the solution of the asymmetric branch. In summary, given the volume difference V_{du} we obtain the pressure drop P_{ud} from Eq. (12) and the sheet's configuration from Eq. (11). This branch no longer exists beyond the critical volume difference provided in Eq. (13b). In Fig. 3 we plot this solution for $\Delta = 0.05$ and for different values of V_{du}/V_{du}^{cr}, and compare the results with the numerical solution of the nonlinear equations, Eqs. (5b), (5c), and (8). To obtain the numerical solution in this branch we set $V_{du} = 0$ in Eq. (7) and place an asymmetric height function as an initial guess. Then we continuously increase the volume difference by a given increment and use the preceding numerical solution as a guess function for the next iteration.

B. Symmetric branch

To obtain the symmetric branch we first calculate the constants a_i and P_y using Eqs. (6c) and (6d). This gives the height profile

$$y(s) = \frac{P_{ud}}{2P_x}(1-s)s + \frac{P_{ud}}{P_x^2}\left[1 - \frac{\cos[\sqrt{P_x}(s-1/2)]}{\cos(\sqrt{P_x}/2)}\right]. \quad (14)$$

Note that at this stage of the analysis the height profile does not converge to the symmetric mode in the limit $P_{ud} \to 0$ because the constant P_x is yet unknown. To determine this constant and the pressure drop P_{ud}, we need to satisfy Eqs. (6b) and (7). These boundary conditions yield the following two transcendental equations:

$$P_{ud} = \frac{16\sqrt{6}u^{7/2}|\cos u|}{\sqrt{6u + 4u(6+u^2)\cos^2 u - 15\sin(2u)}}\Delta^{1/2}, \quad (15a)$$

$$V_{du} = \frac{2\sqrt{2}(u(3+u^2) - 3\tan u)|\cos u|}{\sqrt{3}u^{3/2}\sqrt{6u + 4u(6+u^2)\cos^2 u - 15\sin(2u)}}\Delta^{1/2}, \quad (15b)$$

where $u \equiv \sqrt{P_x}/2$. Given the volume difference V_{du} and the lateral compression Δ, we can solve Eq. (15b) for the constant u, or equivalently P_x, and then substitute this solution in Eq. (15a) to obtain the pressure drop P_{ud}. Therefore, Eqs. (14) and (15) provide the complete solution of the symmetric branch.

Above the maximum volume difference $V_{du} \equiv V_{du}^{max} = \frac{8}{\pi^2}\Delta^{1/2}$ Eq. (15b) does not have a solution, and therefore the symmetric branch with $P_{ud} > 0$ does not exist. At V_{du}^{max} Eq. (15b) admits the lateral compression $P_x = \pi^2$ $(u = \pi/2)$, which gives the pressure drop $P_{ud} = 0$, see Eq. (15a). Indeed, this marginal solution recovers the first, symmetric mode of buckling in Euler's elastica. To show this explicitly we first need to expand Eqs. (15) around $u = \pi/2$, and then solve them perturbatively for P_x and V_{du}. The solutions read

$$P_{ud} \ll 1: \qquad P_x \simeq \pi^2 + \frac{2}{\pi^2}\frac{P_{ud}}{\Delta^{1/2}}, \quad (16a)$$

$$V_{du} \simeq \frac{8}{\pi^2}\Delta^{1/2} - b_1 P_{ud}, \quad (16b)$$

where $b_1 = (216 - \pi^4 - 12\pi^2)/(6\pi^6) \simeq 2.7 \times 10^{-5}$ is a positive constant. Second, we substitute Eq. (16a) in Eq. (14) and take the limit $P_{ud} \to 0$. This gives the height profile $y(s) \to \sqrt{4\Delta/\pi^2}\sin(\pi s)$, which coincides with the symmetric mode of buckling in Euler's elastica. We emphasize that the symmetric branch can also be extended to a region where $V_{du} > V_{du}^{max}$. Nonetheless, this extension requires that $P_{ud} < 0$, and therefore, it will not take place in the spontaneous, quasistatic relaxation of the sheet.

This completes the solution of the symmetric branch. In summary, given the volume difference V_{du} and the lateral compression Δ we need to solve Eq. (15b) to obtain $u = \sqrt{P_x}/2$. Using this solution we calculate the pressure drop in the fluid P_{ud} from Eq. (15a) and the height profile from Eq. (14). In Fig. 4 we plot these height profiles for several values of V_{du} and compare the resulting configurations with the numerical

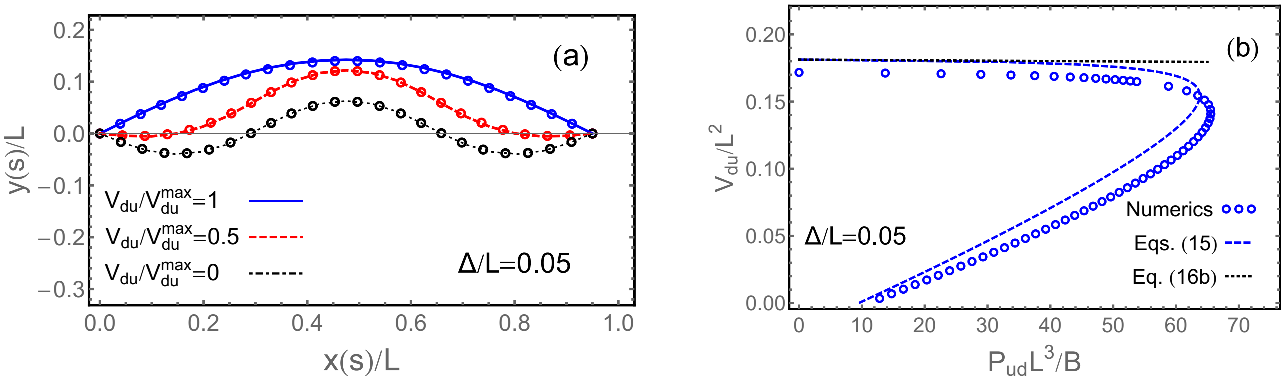

FIG. 4. The evolution of the symmetric branch for $\Delta/L = 0.05$. The explicit normalization is presented in the axes of both panels. (a) The sheet's configuration for several values of the relative volume difference $V_{\text{du}}/V_{\max}$. The maximum volume difference is given numerically by $V_{\text{du}}^{\max}/L^2 \simeq 0.171$ and analytically by $V_{\text{du}}^{\max}/L^2 \simeq 0.181$. Note that the comparison is given for the relative volume difference $V_{\text{du}}/V_{\max}$ and not for the absolute value of V_{du}/L^2. While open circles represent the numerical solution of Eqs. (5b), (5c), and (8) the solid blue, dashed red, and black dotted lines represent the approximated analytical solution, Eqs.(14) and (15) and $x(s) = s - \frac{1}{2}\int_0^s \dot{y}(s')^2 ds'$. When $V_{\text{du}}/V_{\max} = 1$ the system exhibits the first mode of buckling within the theory of Euler's elastica. (b) Comparison between the analytical (dashed blue line) and numerical (open circles) profiles of the P_{ud}-V_{du} relation. The analytical profile is obtained from the solution of Eq. (15). When $P_{\text{ud}} \ll 1$ this profile is approximated by Eq. (16b) (dotted black line).

solution of Eqs. (5b), (5c), and (8). To calculate the symmetric branch numerically, we first set $P_{\text{ud}} = 0$ in Eq. (8) and solve it to obtain $V_{\text{du}}^{\max}$ and its corresponding elastic configuration. Then we reduce the volume difference by a given increment and use the preceding numerical solution as a guess function for the next iteration. Note that when $V_{\text{du}} \to 0$ the symmetric branch converges to a configuration that is close in shape to the third mode of buckling, see Fig. 4(a). In this shape we have from Eqs. (16) that $u \simeq 4.68$ and the pressure drop is $P_{\text{ud}} \simeq 42.5\Delta^{1/2}$. In addition, we plot the numerical P_{ud}-V_{du} relation and compare it with our analytical prediction, Eqs. (15), see Fig. 4(b).

C. Asymmetric-to-symmetric transition

While the lateral force that the chamber applies on the sheet remains constant in the asymmetric branch $P_x = 4\pi^2$, it varies continuously in the symmetric branch, i.e., the parameter $u = \sqrt{P_x}/2$ depends on V_{du} through Eq. (15b). For this reason, we define $m = \sqrt{\pi - u}$ as the order parameter of the asymmetric-to-symmetric transition; when $m = 0$ the system is in the asymmetric branch and when $m > 0$ in the symmetric branch. The control parameter of the transition is defined as the volume difference V_{du}. Note that the definition of the order parameter is valid only in the limit $\Delta \ll 1$, i.e., P_x is not a constant in the asymmetric branch beyond the small amplitude approximation.

In Sec. III A we obtained that above $V_{\text{du}} = V_{\text{du}}^{\text{cr}}$ [see Eq. (13b)] the asymmetric branch ceases to exist. Let us now show that at this critical point the asymmetric-to-symmetric transition occurs, i.e., the energies of the two branches coincide and the order parameter m starts to grow continuously from zero [54].

To obtain the energy of the asymmetric branch we substitute the height profile and the P_{ud}-V_{du} relation, Eqs. (11) and (12), in the energy, Eq. (2), and integrate. Similarly, to obtain the energy of the symmetric branch we utilize Eqs. (14), (15), and (2). In their respected limits these energies read

$$\text{asymmetric}\ \left(V_{\text{du}} < V_{\text{du}}^{\text{cr}}\right):\quad E = \frac{36\pi^2\Delta}{15+2\pi^2} + \frac{P_{\text{ud}}^{\text{cr}}}{2}\left(V_{\text{du}}^{\text{cr}} - V_{\text{du}}\right) - \frac{6\pi^4}{3+\pi^2}\left(V_{\text{du}}^{\text{cr}} - V_{\text{du}}\right)^2, \tag{17a}$$

$$\text{symmetric}\ \left(V_{\text{du}} > V_{\text{du}}^{\text{cr}}\right):\quad E \simeq \frac{36\pi^2\Delta}{15+2\pi^2} - \frac{P_{\text{ud}}^{\text{cr}}}{2}\left(V_{\text{du}} - V_{\text{du}}^{\text{cr}}\right) + \frac{2\pi^4(105+8\pi^2)}{3(15-\pi^2)}\left(V_{\text{du}} - V_{\text{du}}^{\text{cr}}\right)^2, \tag{17b}$$

where $P_{\text{ud}}^{\text{cr}}$ is given by Eq. (13a). Indeed, at $V_{\text{du}} = V_{\text{du}}^{\text{cr}}$ the energies of the two branches coincide. The first derivative of these energies yields the pressure drop in the chamber across the critical point $P_{\text{ud}} = -2dE/dV_{\text{du}}$ [55]

$$\text{asymmetric}\ \left(V_{\text{du}} < V_{\text{du}}^{\text{cr}}\right):\quad P_{\text{ud}} = P_{\text{ud}}^{\text{cr}} - \frac{24\pi^4}{3+\pi^2}\left(V_{\text{du}}^{\text{cr}} - V_{\text{du}}\right), \tag{18a}$$

$$\text{symmetric}\ \left(V_{\text{du}} > V_{\text{du}}^{\text{cr}}\right):\quad P_{\text{ud}} \simeq P_{\text{ud}}^{\text{cr}} - \frac{8\pi^4(105+8\pi^2)}{3(15-\pi^2)}\left(V_{\text{du}} - V_{\text{du}}^{\text{cr}}\right). \tag{18b}$$

Evidently, when $V_{\text{du}} \to V_{\text{du}}^{\text{cr}}$ the pressure drop converges to $P_{\text{ud}} \to P_{\text{ud}}^{\text{cr}}$ from both sides of the transition. Nonetheless, the derivative of the pressure drop (second derivative of the energy) is discontinuous. Note for the sign change and the relatively big jump of this derivative. While $dP_{\text{ud}}/dV_{\text{du}} \simeq 181$ in the asymmetric branch, it changes into $dP_{\text{ud}}/dV_{\text{du}} \simeq -9313$ in

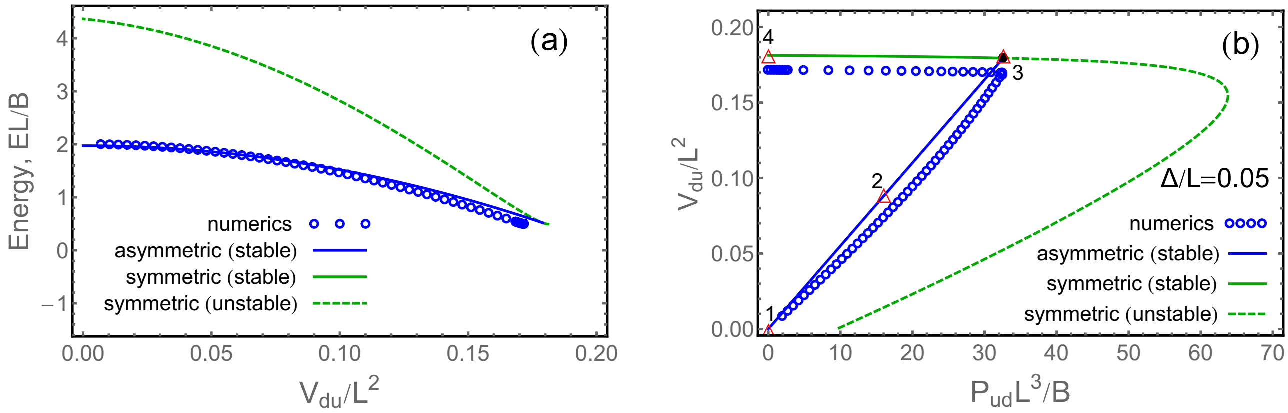

FIG. 5. Comparison between the approximated solution and the numerical minimization of the total energy. In both panels $\Delta/L = 0.05$ and the axes are presented in the explicit normalization. In addition, open-blue circles represent the numerical values, solid blue line the analytical approximation of the asymmetric branch, and solid green and dashed green (light gray) lines the analytical approximation of the symmetric branch. (a) The normalized elastic energy EL/B is plotted as a function of the normalized volume difference V_{du}/L^2. Theoretically, the energy of the asymmetric branch is calculated from Eqs. (2), (11), and (12), and the energy of the symmetric branch from Eqs. (2), (14), and (15). The asymmetric branch is energetically favorable over the symmetric branch when $V_{\mathrm{du}}/V_{\mathrm{du}}^{\mathrm{cr}} < 1$. At $V_{\mathrm{du}}/V_{\mathrm{du}}^{\mathrm{cr}} = 1$ the asymmetric branch ceases to exist and the symmetric branch becomes stable. Since $V_{\mathrm{du}}^{\mathrm{cr}}/V_{\max} \simeq 0.99$ the region in which the symmetric branch is stable is hardly seen in this figure. Discrepancies between the numerical and analytical predictions are attributed to the finite size of the sheet. (b) Comparison between the numerical and analytical P_{ud}-V_{du} relations. Numerically, the pressure drop is obtained from $P_{\mathrm{ud}} = -2dE/dV_{\mathrm{du}}$, where E is given in panel (a). Analytically, the P_{ud}-V_{du} relation is given by Eq. (12) for the asymmetric branch and by Eqs. (15) for the symmetric branch. Note that P_{ud} is continuous at the transition, but its first derivative is discontinuous, see Eq. (18). To visualize the evolution of the elastic configuration as V_{du}/L^2 is increasing, we added four labels (red triangles) that correspond, in part, to the shapes presented in Figs. 3(a) and 4(a). While labels $1\ldots3$ along the asymmetric branch mark the three shapes presented in Fig. 3(a), label 4 in the symmetric branch corresponds to $V_{\mathrm{du}}/V_{\mathrm{du}}^{\max} = 1$ in Fig. 4(a). Note that, despite the relatively large change in the pressure difference between labels 3 and 4, the elastic configuration barely changes.

the symmetric branch. Lastly, to obtain the order parameter m close to the transition we substitute $u = \pi - m^2$ in Eq. (15b) and expand it to leading order in m. This gives

$$m \simeq \sqrt{\frac{2\pi(3+\pi^2)(15+2\pi^2)}{9(15-\pi^2)}}\left(\frac{V_{\mathrm{du}} - V_{\mathrm{du}}^{\mathrm{cr}}}{V_{\mathrm{du}}^{\mathrm{cr}}}\right)^{1/2}, \tag{19}$$

with a critical exponent of $\beta = 1/2$ that is expected from a continuous second-order transition.

To verify the analytical analysis of this transition, we compare our results with the numerical minimization of the total energy, Eq. (2). This numerical minimization is carried out using the built-in function FINDMINIMUM in MATHEMATICA© [56], where the elastic sheet is discretized into $N = 70$ equally spaced points, and Eqs. (1) and (7) are considered as external constraints.

The results of this numerical analysis is presented in Fig. 5 and compared with the approximated solution derived in Secs. III A and III B. In Fig. 5(a) we plot the total elastic energy of the numerical solution and compare it with the energies of the asymmetric and symmetric branches. We find that the global minimizer of the system follows the asymmetric branch until it ceases to exist. Discrepancies between the numerical and analytical energies are attributed to the finite size of the sheet, i.e., break down of the assumption that $\Delta \ll 1$. In Fig. 5(b) we plot the numerical P_{ud}-V_{du} relation and compare it with the analytical prediction. When $V_{\mathrm{du}} < V_{\mathrm{du}}^{\mathrm{cr}}$ the asymmetric branch dominates the system and the P_{ud}-V_{du} relation is approximated by Eq. (12). At $V_{\mathrm{du}} = V_{\mathrm{du}}^{\mathrm{cr}}$ the asymmetric branch ceases to exist and the transition occurs. While P_{ud} is continuous across the transition, its first derivative is discontinuous. Beyond the critical point the P_{ud}-V_{du} relation follows the symmetric branch, Eqs. (15). Note that the asymmetric branch dominates the evolution of the system up to $V_{\mathrm{du}}^{\mathrm{cr}}/V_{\mathrm{du}}^{\max} \simeq 0.987$, which is similar to our analytical approximation $V_{\mathrm{du}}^{\mathrm{cr}}/V_{\mathrm{du}}^{\max} \simeq 0.99$, where $V_{\mathrm{du}}^{\mathrm{cr}}$ is given by Eq. (13b) and $V_{\mathrm{du}}^{\max} = \frac{8}{\pi^2}\Delta^{1/2}$. To follow the configuration of the sheet along the stable trajectory of the system, we added labels to Fig. 5(b) that mark the corresponding shapes in Figs. 3(a) and 4(a). Note that, although the pressure difference changes considerably in the symmetric branch, the elastic configuration almost remains unchanged, compare the shapes corresponding to labels 3 and 4 in Fig. 5(b).

IV. NUMERICAL INVESTIGATION BEYOND THE SMALL AMPLITUDE APPROXIMATION

In this section we minimize the elastic energy numerically in a region of the parameter space that goes beyond the small amplitude approximation. We emphasize that, different from previous sections, where we normalized all lengths by L and vary L_x, here, we fix the lateral dimension of the chamber, say $L_x = 1$, and vary the total length of the sheet. We show that under these conditions the critical pressure drop at the asymmetric-to-symmetric transition $P_{\mathrm{ud}}^{\mathrm{cr}}(L/L_x)$ behaves nonmonotonically.

This section is divided into three parts. In the first part, we investigate the numerical solution of our model at relatively large values of L/L_x. In the second part, we modify the boundary conditions on the sheet's edges from hinged to clamped,

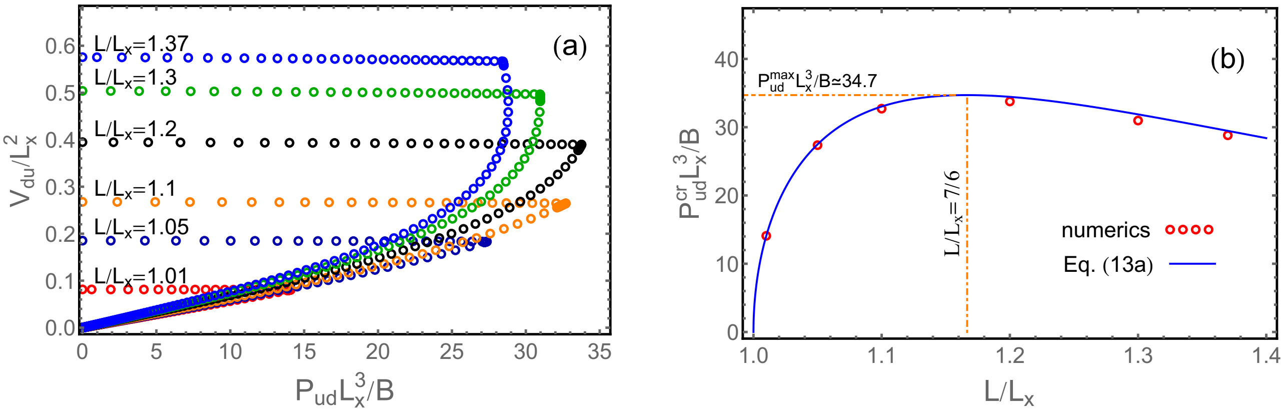

FIG. 6. Numerical investigation beyond the small amplitude approximation. The explicit normalization is presented in the axes of both panels. (a) The P_{ud}-V_{du} relation for different total lengths L/L_x. In all cases the pressure drop increases from zero up to some critical value that marks the asymmetric-to-symmetric transition and then quickly decreases to zero. Despite the rapid reduction to zero the transition is always of a second order, i.e., P_{ud} is continuous at the transition, but its first derivative is discontinuous. (b) The critical pressure drop as a function of L/L_x. While open-red circles correspond to the critical pressures obtained in panel (a), the blue line corresponds to the analytical approximation, Eq. (13a). The $P_{\mathrm{ud}}^{\mathrm{cr}}L_x^3/B$ is maximized at a critical length, $L/L_x \simeq 1.16$, which agrees nicely with the analytical prediction.

and show that this modification affects only quantitatively the behavior of the system. Lastly, we examine the efficiency of our proposed apparatus and discuss the effect of the boundary conditions on this quantity.

A. Hinged sheets

In this section we investigate the behavior of the system numerically, beyond the small amplitude approximation. To do that, we fix the lateral length of the chamber $L_x = 1$ and minimize the elastic energy Eq. (2) numerically over a wide range of L/L_x. In each run we record the spatial configuration of the sheet and the P_{ud}-V_{du} relation. First, we find that contact between the sheet and the side walls of the chamber occurs when $L/L_x \simeq 1.37$ (we assume that L_y is large enough). Therefore, the following discussion is restricted to the range $L/L_x \in [1, 1.37]$.

In Fig. 6(a) we plot the P_{ud}-V_{du} relation for several values of L/L_x. This plot indicates that the behavior of the sheet remains qualitatively unchanged compared with the small amplitude approximation. This similarity is manifested in the following two observations. (i) The system always exhibits a continuous asymmetric-to-symmetric transition. Although P_{ud} is continuous at the critical point, its first derivative is discontinuous. (ii) The asymmetric branch dominates most of the system's evolution, i.e., the transition occurs very close to $V_{\mathrm{du}}^{\mathrm{max}}$. Despite these two similarities, we note that when $L/L_x \gtrsim 1.1$ the P_{ud}-V_{du} relation in the asymmetric branch is no longer linear, different from our prediction in Eq. (12).

Interestingly, Fig. 6(a) reveals that the critical pressure drop $P_{\mathrm{ud}}^{\mathrm{cr}}$ behaves nonmonotonically as a function of the lateral compression L/L_x. It increases when $L/L_x \lesssim 1.1$ and decreases beyond it. In Fig. 6(b) we plot the critical pressure as a function of L/L_x and fit it with Eq. (13a). Retrieving dimensions into the latter equation and rescale L by L_x we obtain, $P_{\mathrm{ud}}L_x^3/B = \sqrt{\frac{768\pi^6}{15+2\pi^2}}\frac{[(L/L_x)-1]^{1/2}}{(L/L_x)^{7/2}}$, where we replaced the pressure difference with $P_{\mathrm{ud}} \rightarrow P_{\mathrm{ud}}L^3/B$ and we used the definition of the normalized lateral compression $\Delta = 1 - L_x/L$. Although this region of the system is much beyond the strict limits of our approximated theory we observe that it fits well with the numerical values. This observation allows us to estimate the maximum pressure drop that the system acquires under hinged boundary conditions. Solving $dP_{\mathrm{ud}}^{\mathrm{cr}}/dL = 0$ gives $L/L_x = 7/6$, and the maximum pressure drop $P_{\mathrm{ud}}^{\mathrm{max}}L_x^3/B = \frac{3456\pi^3}{343}\sqrt{\frac{3}{7(15+2\pi^2)}} \simeq 34.7$.

B. Clamped sheets

To verify that our qualitative understanding of the system remains valid even when the boundary conditions on the sheet's edges are modified, we replace Eqs. (6d) with clamped boundary conditions, i.e., the tangent angle is zero at the boundary, and minimize the elastic energy numerically. First, we observe that self-contact occurs at $L/L_x \simeq 2.9$. Therefore, our investigation is focused on lower values of the total length, see Fig. 7.

In Fig. 7(a) the configuration of the sheet is plotted for several values of $V_{\mathrm{du}}/V_{\mathrm{du}}^{\mathrm{max}}$ when $L/L_x = 1.5$. As expected, both of the limiting solutions at $V_{\mathrm{du}} = 0$ and $V_{\mathrm{du}}/V_{\mathrm{du}}^{\mathrm{max}} = 1$, coincide with the second (asymmetric) and the first (symmetric) modes of buckling in the framework of Euler's elastica, and therefore satisfy $P_{\mathrm{ud}} = 0$. The complete P_{ud}-V_{du} relations in between the two limiting solutions are plotted in Fig. 7(b) for several values of L/L_x. Similar to hinged sheets, the pressure drop in the chamber increases monotonically up to some maximum value that coincides with the critical pressure at which the asymmetric-to-symmetric transition occurs. Beyond the critical point the pressure drop decreases to zero. At the transition the pressure drop remains continuous but its first derivative is discontinuous. Nonetheless, note that in the case of clamped sheets the symmetric branch dominates the system at much wider region compared with hinged sheets.

Finally, we notice that the critical pressure drop in the chamber $P_{\mathrm{ud}}^{\mathrm{cr}}$ behaves nonmonotonically as a function of

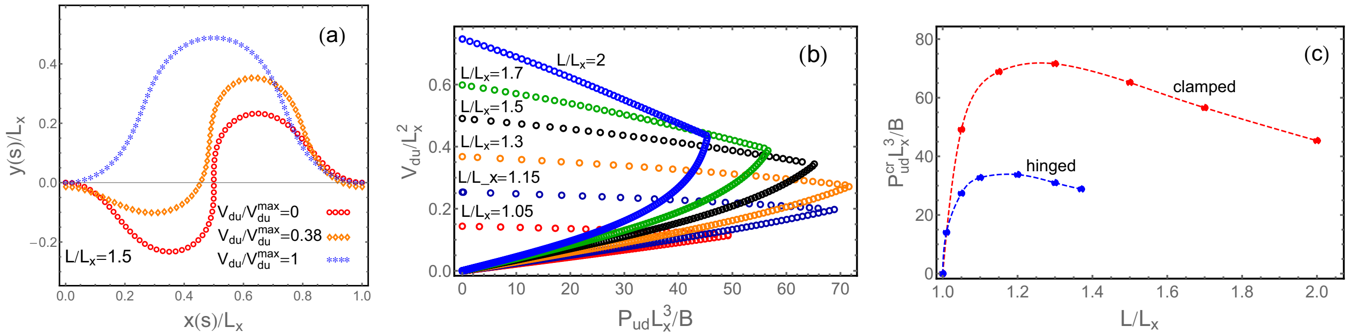

FIG. 7. Numerical investigation of a sheet that is clamped at both ends. The explicit normalization is presented on the axes of all panels. (a) The configuration of the sheet for several values of the volume ratio $V_{\rm du}/V_{\rm du}^{\rm max}$ ($V_{\rm du}^{\rm max}/L_x^2 = 0.49$) and for $L/L_x = 1.5$. The system exhibits the second and first modes of buckling when $V_{\rm du}/V_{\rm du}^{\rm max} = 0$ and $V_{\rm du}/V_{\rm du}^{\rm max} = 1$, respectively. (b) The $P_{\rm ud}$-$V_{\rm du}$ relations for several values of L/L_x. In all cases the pressure drop increases from zero up to a critical value, which coincides with the the asymmetric-to-symmetric transition, and then decreases back to zero. While the pressure drop is continuous at the transition its first derivative is discontinuous. (c) The normalized critical pressure drop is plotted as a function of L/L_x. The case of a hinged sheet is plotted for comparison where the data points are taken from Fig. 6(b). While dots corresponds to the numerical values, dashed lines are their interpolations. Qualitatively, in both cases of the boundary conditions, the sheet exhibits the same nonmonotonic dependence. However, the maximum pressure drop in clamped sheets is higher by approximately a factor of two compared with hinged sheets.

L/L_x. This behavior is depicted in Fig. 7(c) where the maximum pressure drop $P_{\rm ud}^{\rm cr}L_x^3/B \simeq 71$ is obtained at $L/L_x \simeq 1.22$; compare these values with $P_{\rm ud}^{\rm cr}L_x^3/B \simeq 34.7$ and $L/L_x \simeq 1.16$ obtained for hinged sheet.

C. Energy difference and efficiency

The difference in energy between the two limiting solutions essentially determines the total amount of work that our apparatus can perform, i.e., $\Delta E \equiv E_2 - E_1 = \frac{1}{2}\int_0^{V_{\rm du}^{\rm max}} P_{\rm ud}(V_{\rm du})dV_{\rm du}$, where E_2 and E_1 are the energies of the second and the first modes of buckling, and we keep in mind that $P_{\rm ud} = -2dE/dV_{\rm du}$. Accordingly, we can define the efficiency of this apparatus as the fraction of the elastic energy, relative to E_2 that is exploited to displace the fluid, i.e., $\eta \equiv \Delta E/E_2$. In Fig. 8 we plot these two quantities, ΔE and η, as a function of L/L_x for clamped and hinged sheets.

We mention three main findings regarding these plots. First, the energy difference is higher for clamped sheets compared with hinged sheets for all values of L/L_x. Second, while for hinged sheets ΔE increases monotonically, for clamped sheets we observe nonmonotonic behavior. Yet the critical length at which the energy difference is maximized differs from the critical length observed for $P_{\rm ud}^{\rm cr}$, see Fig. 7(c). Third, in both cases the efficiency depends only weakly on L/L_x. In addition, the efficiency of hinged sheets is higher ($\eta \simeq 0.75$) compared with clamped sheets ($\eta \simeq 0.5$).

V. CONCLUSION

In this paper we studied a mechanical system that converts the elastic energy stored in a thin body into a hydrodynamic pressure that potentially can trigger a flow. We derived an analytical model that predicts the slow, quasistatic, evolution of

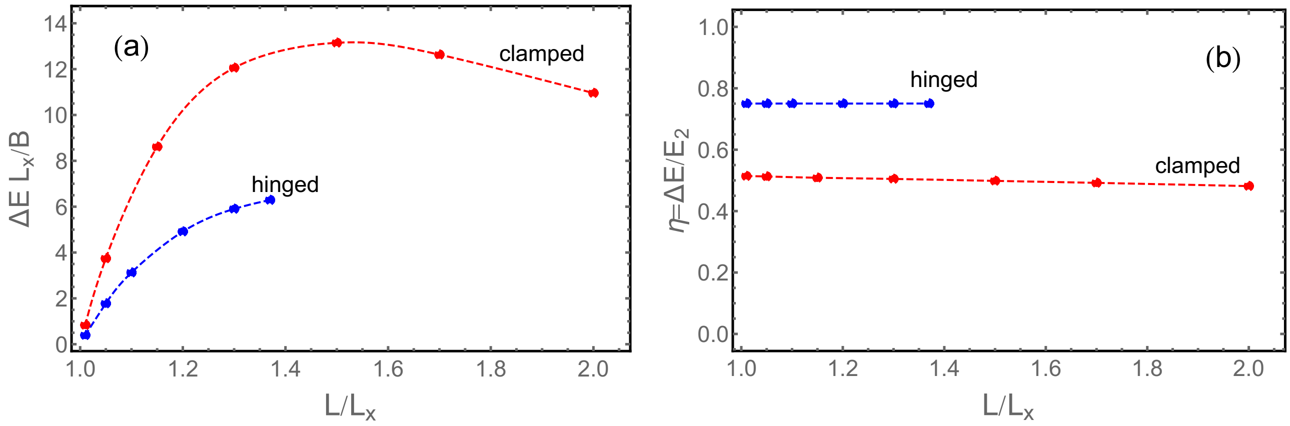

FIG. 8. Energy difference and efficiency for hinged and clamped sheets. The explicit normalization is presented in both panels. In addition, dots correspond to the numerical data and dashed lines to the interpolation between them. (a) The difference in energy between the two limiting solutions is plotted as a function of L/L_x. Clamped sheets have a higher energetical barrier between the first two modes of buckling, compared with hinged sheets. In addition, this energy difference behaves nonmonotonically in the case of clamped sheets. (b) Efficiency as a function of L/L_x. Hinged sheets are more efficient than clamped sheets. In both cases η decreases only slightly with an increase in L/L_x.

the system given the volume difference between the two sides of the chamber. Assuming that the lateral compression remains small and that the sheet's edges were hinged to the side walls of the chamber, we obtained an analytical and tractable solution to our model. This solution revealed that the system progresses between two different branches of solutions, an asymmetric branch and a symmetric branch. The asymmetric branch dominates the system as long as it is available, and once it ceases to exist the symmetric branch becomes energetically favorable. We showed that the transition between the two branches is continuous, i.e., of a second order.

Furthermore, we investigated the numerical solution of our model at moderate values of the lateral compression for both hinged and clamped sheets. We showed that in both cases our qualitative understanding of the system, as depicted in the small amplitude approximation, remains valid. Nonetheless, we found that when the lateral compression is large the $P_{\rm ud}$-$V_{\rm du}$ relation is no longer linear. In addition, we showed that when we fixed L_x and varied the total length of the sheet, the critical pressure drop at which the transition occurred behaves nonmonotonically as a function of L/L_x, i.e., $P_{\rm ud}^{\rm cr}$ was maximized at $L/L_x \simeq 1.16$ for hinged sheets and $L/L_x \simeq 1.22$ for clamped sheets. Furthermore, we showed that, although the energetic gap between the two first modes of buckling in clamped sheets is larger than in hinged sheets, the latter boundary conditions were more efficient.

To get some physical intuition regarding the magnitude of the pressure drop our system can acquire, assume that the width of the chamber is $L_x = 5\,{\rm cm}$ (L_y does not affect the calculation) and the elastic sheet is made of PVS with Young's modulus $\tilde{E} \simeq 790\,{\rm KPa}$, Poisson's ratio $\nu = 0.4$, and thickness $t = 3\,{\rm mm}$, similar to the material used in Ref. [48]. In addition, suppose that the sheet is hinged to the side walls of the chamber and its total length equals $L = (7/6)L_x$, such that the pressure drop is maximized at the asymmetric-to-symmetric transition. Under these conditions the maximum pressure drop in the chamber would be $P_{\rm ud}^{\rm cr} \simeq 35B/L_x^3 \simeq 600\,{\rm Pa}$. Neglecting all viscous effects and assuming that the fluid is made of water, this pressure drop can potentially yield the fluid's velocity $v = \sqrt{2P_{\rm ud}^{\rm cr}/\rho} \simeq 1.1\,{\rm m/s}$, where $\rho = 1 \times 10^3\,{\rm kg/m^3}$ is the fluid's density. Obviously, this velocity depends strongly on the bending modulus of the sheet and the lateral dimension of the chamber.

The pressure difference induced in the chamber can potentially be exploited to perform work on external objects. Here we mention three such potential applications. First, suppose that the channel connecting the two parts of the chamber is endowed with a flexible beam, as considered, for example, in Refs. [42,46] that is coated with piezoelectric patches [20]. The pressure difference in the chamber will then be exploited to displace the beam and to induce an electric voltage. Of course, we must keep in mind that any external object that is added to our device can affect its expected operation including changes in the $P_{\rm du}$-$V_{\rm du}$ relation, reduced efficiency, and qualitative changes in the bifurcation diagrams.

The second application is related to the design of micropumps that are of interest in the research of microfluidics [57,58]. Since our device stores elastic energy that scales with the thickness of the material, the energetic difference between two consecutive modes of buckling significantly decreases with a reduce in the thickness. Therefore, the device can potentially store and release very small, but highly accurate, amount of fluid in each loading cycle. This accuracy can be utilized, for example, to pump liquids or nanosized particles through microchannels. Lastly, we suggest that our apparatus can be utilized as a microfluidic mixing device [59], i.e., if the two parts of the chamber are filled with different fluids, the elastic energy released from the sheet can be exploited to mix between them. Of course, we keep in mind that these applications will most probably operate more efficiently when dynamic effects are taken under consideration. Nonetheless, our quasistatic analysis provides guidelines to the design of such applications.

An interesting observation raised in this study suggests that the maximum pressure drop in the chamber depends strongly on the boundary conditions. Indeed, $P_{\rm ud}^{\rm cr}$ in clamped sheets is almost double compared to its value in the case of hinged sheets. One can then formulate a problem in variational elasticity and ask which boundary conditions maximize the pressure drop in the chamber. Along the same lines, another interesting question would be to investigate which boundary conditions maximize the energetic gap between the first two modes of buckling and the efficiency of the device.

Despite the progress made here our study did not consider the inevitable dynamic effects and pressure loss due to friction, which will take place in any design of such energy harvesting device. Therefore, our future study will focus on the incorporation of these effects into the analytical model, i.e., add inertial terms into the force balance equations describing the coupled motion of the fluid and of the elastic sheet.

We hope that the proposed setup would be useful to elucidate the fundamental behavior of the snap-through mechanism in a viscous medium. For example, it would be interesting to investigate how viscosity affects the growth rate of the instability. Hopefully, the answer to these fundamental questions will lay the groundwork for advanced technological applications that exploit the snap-through instability to the design of mechanical switches [19,60–62], or memcapacitors in electrical circuits [63,64].

ACKNOWLEDGMENTS

We thank Benny Davidovitch, Lior Atia, and Yuri Feldman for stimulating discussions. This work was supported, in part, by the Pearlstone Center for Aeronautical Studies.

APPENDIX A: EVOLUTION OF A PRESSURE-CONTROLLED SYSTEM

In this Appendix we examine the evolution of the system when the pressure difference, instead of the volume difference, is the control parameter. To do that, we slightly modify the schematic overview of the system, Fig. 1, and consider a chamber that is endowed with two pistons at its upper and bottom walls. These pistons fix the upper and lower pressures, $P_{\rm u}$ and $P_{\rm d}$, respectively, as seen in Fig. 9. Initially we set $P_{\rm u} = P_{\rm d}$ ($P_{\rm ud} = 0$), and then we increase the upper pressure while keeping the lower pressure fixed, i.e., $P_{\rm ud} \geqslant 0$. Given the properties of the sheet, L and B, the dimensions of the

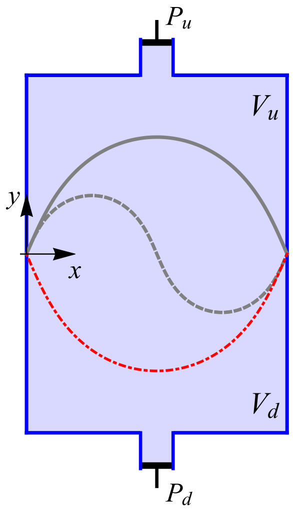

FIG. 9. Schematic overview of the pressure-controlled system. A closed rectangular chamber is filled with an incompressible fluid and is divided into two parts by a thin sheet. The dimensions of the chamber and the properties of the sheet remain unchanged compared to the main text. The pressures above and below the elastic sheet, P_u and P_d, are determined by the upper and lower pistons. When $P_\mathrm{ud} \geqslant 0$, the system exhibits three different branches of solutions, an unstable asymmetric branch (dashed gray line), a meta-stable symmetric branch (solid gray line) and an inverted-symmetric branch (dashed-dotted red line), which is globally stable.

chamber $L_x \times L_y$, and the pressure difference P_ud, we wish to find the spatial orientation of the sheet. Note that, different from the main text, in this Appendix the shape changes of the sheet are not a result of a spontaneous process but they are driven by the external pressures.

The elastic energy to be minimized under this setup has two contributions. One from the bending energy of the sheet, similar to Eq. (2), and second from the mechanical work performed on the system by the external pressures. Following our normalization convention in Sec. II the total energy is given by

$$E_\mathrm{pc} = \frac{1}{2}\int_0^1 \dot{\phi}^2 ds - P_\mathrm{u}V_\mathrm{u} - P_\mathrm{d}V_\mathrm{d}$$
$$= \int_0^1 \left(\frac{1}{2}\dot{\phi}^2 + \frac{P_\mathrm{ud}}{2}\mathbf{x}\cdot\hat{\mathbf{n}}_\mathrm{d}\right)ds + E_0, \qquad \text{(A1)}$$

where $E_0 \equiv -P_\mathrm{u}L_xL_y$ is a constant, and to derive the second equality we used Eq. (3) and the relation $V_\mathrm{u} + V_\mathrm{d} = L_xL_y$.

Keeping in mind the geometric constraints, Eqs. (1), minimization of the energy, Eq. (A1), with respect to the elastic fields gives the same set of equilibrium equations as derived in the case of a volume-controlled deformation, Eqs. (5) and (6). Nonetheless, since P_ud is now a known parameter, the condition that relates the elastic shape to the volume difference, Eq. (7), is unnecessary to form a closure.

Following the analysis in Sec. III, we investigated the minimizers of the energy in the limit of the small amplitude approximation. We identified three different branches of solutions that govern the system. One is the asymmetric branch that we derived in Sec. III A, second is the symmetric branch derived in Sec. III B, and third is the inverted-symmetric branch. The latter branch is just the mirror solution of the symmetric branch, see Fig. 9. This inverted shape did not play a role in our volume-controlled investigation because we only considered cases in which $V_\mathrm{du} > 0$ (and $P_\mathrm{ud} > 0$). In this Appendix the control parameter is $P_\mathrm{ud} \geqslant 0$, and therefore V_du can, in general, take negative values.

The elastic configurations of the symmetric and inverted-symmetric branches are given by Eqs. (14) and (15a). When $P_\mathrm{ud} > 0$ Eq. (15a) has two different solutions, one with $u \geqslant \pi/2$, which corresponds to the symmetric branch, and second with $u \leqslant \pi/2$ that yields the inverted branch [65].

To analyze the stability of the system with respect to the three branches, we first calculate their total energy. In the small amplitude approximation Eq. (A1) reduces to $E_\mathrm{pc} - E_0 = \int_0^1 (\frac{1}{2}\ddot{y}^2 + P_\mathrm{ud}y)ds$ and the energies read

$$\text{asymmetric:} \quad E_\mathrm{pc} = 4\pi^2\Delta + \frac{(3+\pi^2)P_\mathrm{ud}^2}{96\pi^4}, \qquad \text{(A2a)}$$

$$\text{symmetric/inverted-symmetric:} \quad E_\mathrm{pc} = \frac{6u + 4u(9+2u^2)\cos^2 u - 21\sin(2u)}{384u^5\cos^2 u}P_\mathrm{ud}^2. \qquad \text{(A2b)}$$

While the energy of the asymmetric branch, Eq. (A2a), exhibits the explicit dependence on the control parameter P_ud, the energies of the symmetric and inverted-symmetric branches are given parametrically, i.e., given P_ud we need to solve Eq. (15a) for $u = \sqrt{P_x}/2$ and then substitute this solution back in Eq. (A2b).

Figure 10 presents the typical evolution of the system for the case where $\Delta = 0.05$. In Fig. 10(a) we plot the energies of the three branches. When $P_\mathrm{ud} = 0$ the system has three potential minimizers. One is the second mode of buckling, and the other two are the first mode of buckling with the sheet either oriented upwards or downwards, see Fig. 9. Indeed, when the pressure difference vanishes, these three minimizers coincide with the modes of buckling in the theory of Euler's elastica. The local stability of these solutions has been investigated, for example, in Ref. [66], who showed that while the second mode of buckling is unstable, the first mode of buckling is stable and represents the minimum of the energy. Therefore, we would initially expect the system to accommodate either the symmetric branch or the inverted-symmetric branch.

When $P_\mathrm{ud} > 0$ the energies of the latter minima splits. While the energy of the symmetric branch increases, i.e., it becomes a metastable state, the energy of the inverted-symmetric branch decreases, i.e., it remains the global minimizer. Therefore, had the system initially been in the inverted-symmetric state, it would have stayed in this branch for any $P_\mathrm{ud} > 0$. However, had the system initially been in the symmetric branch, the behavior would have been more

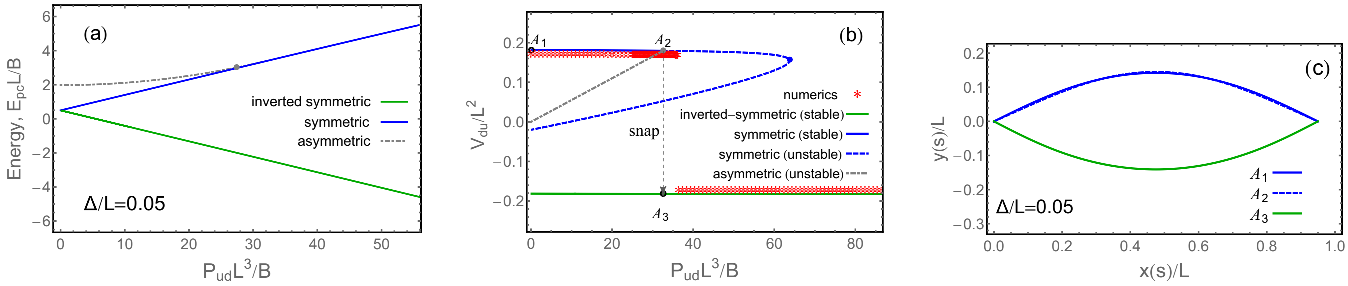

FIG. 10. Typical evolution of the pressure-controlled system. The explicit normalization is presented on the axes in all panels. (a) The normalized energy, Eq. (A1), as a function of the normalized control parameter $P_{\rm ud}L^3/B$. While the energy of the asymmetric branch is given by Eq. (A2a), the energies of the symmetric and inverted-symmetric branches are given by Eqs. (A2b) and (15a). The asymmetric branch is always higher in energy compared to the other branches. While the energies of the symmetric and inverted-symmetric branches coincide at $P_{\rm ud}=0$, they deviate for any $P_{\rm ud}>0$. While the symmetric branch represents a local minimum of the energy (metastable solution), the inverted-symmetric branch represents the global minimum, i.e., it has the lowest energy among all three branches. (b) The $P_{\rm ud}$-$V_{\rm ud}$ relations for the three branches. Had the system initially been in the symmetric branch (the point A_1), it would have remained in this branch (solid blue line) until the system crossed some energetic barrier. Numerical investigation shows that this happens very close to $P_{\rm ud}^{\rm cr}$ (the point A_2). (c) One possible evolution of the elastic configuration form A_1 to A_2 in the symmetric branch, and then a snap to A_3 in the inverted branch [see panel (b)]. Note that there is almost no change in the elastic shape when the system evolves along the symmetric branch.

complex, and would resemble the evolution of a von Mises truss [37,67]. Namely, the system can remain in the local minimum until it overcomes some energetic barrier, or until the symmetric branch ceases to exist, see the so-called limit point in Fig. 10(b). The difference between the two scenarios are discussed in Ref. [40]. Numerical minimization of the energy indicates that the symmetric branch becomes unstable close to the intersection with the unstable asymmetric branch, i.e., close to the critical pressure difference $P_{\rm ud}^{\rm cr}$, Eq. (13a).

APPENDIX B: EXACT SOLUTION TO EQ. (8)

To derive the exact solution of the problem we first manipulate Eq. (8) to describe the balance of forces over an infinitesimal (rather than finite) length of the sheet. To do that, we multiply Eq. (8) with $\dot\phi$ and integrate the equation with respect to s. This gives the following constant:

$$\mathcal{H}=\frac{1}{2}\dot\phi^2+P_{\rm ud}(x\sin\phi-y\cos\phi)-P_x\cos\phi-P_y\sin\phi, \tag{B1}$$

which is conserved over the spatial configuration of the sheet, i.e., $\mathcal{H}$ is independent of s. Then we differentiate Eq. (8) with respect to s and utilize Eq. (B1) to simplify the result. This gives

$$\dddot\phi+\left(\frac{1}{2}\dot\phi^2-\mathcal{H}\right)\dot\phi+P_{\rm ud}=0. \tag{B2}$$

Equation (B2) describes the balance of normal forces on an infinitesimal element of the sheet. The investigation of this equation has been the subject of many recent studies that are related to cylindrical configurations of fluid membranes [51,68,69], folding of pressurized rings [70,71], deformation of a carbon nanotube [72], and the mathematical investigation of area-constrained elastica [50,73,74].

Not only does Eq. (B2) acquire an exact solution in terms of the Jacobi Elliptic functions, its corresponding embeddings, i.e., the configuration on the xy plane, are given as a function of the tangent angle $\phi(s)$ and its derivatives alone [68]. Indeed, we can exploit Eqs. (8) and (B1) to obtain the following trajectory:

$$x(s)=-\frac{\ddot\phi}{P_{\rm ud}}\cos\phi-\frac{\dot\phi^2-2\mathcal{H}}{2P_{\rm ud}}\sin\phi+x_o, \tag{B3a}$$

$$y(s)=-\frac{\ddot\phi}{P_{\rm ud}}\sin\phi+\frac{\dot\phi^2-2\mathcal{H}}{2P_{\rm ud}}\cos\phi+y_o, \tag{B3b}$$

where the constants x_o and y_o correspond to a rigid shift of the elastic shape, and are yet to be determined by the boundary conditions.

Following Ref. [51] the solution of Eq. (B2) is given by

$$\begin{aligned}\phi(s)={}&\frac{A\beta-B\alpha}{A-B}s+\frac{(A+B)(\alpha-\beta)}{2u(A-B)}\\&\times\Pi\left(-\frac{(A-B)^2}{4AB},\,\mathrm{am}(us+c,k^2),\,k^2\right)\\&+\frac{\alpha-\beta}{2u\sqrt{k^2+\frac{(A-B)^2}{4AB}}}\arctan\\&\times\left(\sqrt{k^2+\frac{(A-B)^2}{4AB}}\,\frac{\mathrm{sn}(us+c,k^2)}{\mathrm{dn}(us+c,k^2)}\right)+\bar\phi,\end{aligned} \tag{B4}$$

where $\bar\phi$ and c are arbitrary constants, and the functions cn, am, dn, and Π denote the elliptic functions [49,56,75]. In addition, the various constants used in Eq. (B4) are given by

$$u=\frac{\sqrt{AB}}{4},\ A=\sqrt{4\eta^2{+}(3\alpha+\beta)^2},\ B=\sqrt{4\eta^2{+}(\alpha{+}3\beta)^2},$$
$$k^2=\frac{1}{2}-\frac{4\eta^2+(3\alpha+\beta)(\alpha+3\beta)}{2AB}, \tag{B5}$$

where α, β, and η are related to the roots of the polynomial $P(\kappa)=2e-\frac{1}{4}\kappa^4+\mathcal{H}\kappa^2-2P_{\rm ud}\kappa$, and e is an unknown constant. While α and β ($\alpha<\beta$) correspond to the real roots of $P(\kappa)$, the parameter η equals the imaginary part of the complex conjugate pair of $P(\kappa)$.

This completes the analytical solution. In summary, to obtain the configuration of the sheet on the

xy plane we first need to determine the constants $\{x_o, y_o, \mathcal{H}, \bar{\phi}, c, e, P_{\text{ud}}\}$ from the solution of the boundary conditions, Eqs. (6) and (7). Then we can substitute these constants in the tangent angle, Eqs. (B4) and (B5), and utilize it to obtain the configuration from Eq. (B3).

[1] E. Cerda and L. Mahadevan, Phys. Rev. Lett. **90**, 074302 (2003).

[2] B. Davidovitch, R. D. Schroll, D. Vella, M. Adda-Bedia, and E. A. Cerda, Proc. Natl. Acad. Sci. **108**, 18227 (2011).

[3] H. Diamant and T. A. Witten, Phys. Rev. Lett. **107**, 164302 (2011).

[4] O. Oshri, F. Brau, and H. Diamant, Phys. Rev. E **91**, 052408 (2015).

[5] Y. Klein, E. Efrati, and E. Sharon, Science **315**, 1116 (2007).

[6] Y. Klein, S. Venkataramani, and E. Sharon, Phys. Rev. Lett. **106**, 118303 (2011).

[7] D. Holmes and A. Crosby, Adv. Mater. **19**, 3589 (2007).

[8] H. King, R. D. Schroll, B. Davidovitch, and N. Menon, Proc. Natl. Acad. Sci. **109**, 9716 (2012).

[9] T. A. Witten, Rev. Mod. Phys. **79**, 643 (2007).

[10] T. Tallinen, J. A. Åström, and J. Timonen, Nat. Mater. **8**, 25 (2009).

[11] D. P. Holmes, Curr. Opin. Colloid Interface Sci. **40**, 118 (2019).

[12] E. Efrati, E. Sharon, and R. Kupferman, J. Mech. Phys. Solids **57**, 762 (2009).

[13] B. Roman and J. Bico, J. Phys.: Condens. Matter **22**, 493101 (2010).

[14] O. Oshri, S. Biswas, and A. C. Balazs, Phys. Rev. E **100**, 043001 (2019).

[15] O. Oshri, S. Biswas, and A. C. Balazs, Phys. Rev. E **99**, 033003 (2019).

[16] O. Oshri, S. Biswas, and A. C. Balazs, Phys. Rev. E **102**, 033004 (2020).

[17] M. Pezzulla, S. A. Shillig, P. Nardinocchi, and D. P. Holmes, Soft Matter **11**, 5812 (2015).

[18] O. Oshri and H. Diamant, Phys. Rev. E **95**, 053003 (2017).

[19] P. Rothemund, A. Ainla, L. Belding, D. J. Preston, S. Kurihara, Z. Suo, and G. M. Whitesides, Science Robotics **3**, eaar7986 (2018).

[20] R. L. Harne and K. W. Wang, Smart Mater. Struct. **22**, 023001 (2013).

[21] C. R. Bowen, H. A. Kim, P. M. Weaver, and S. Dunn, Energy Environ. Sci. **7**, 25 (2014).

[22] N. Hu and R. Burgueño, Smart Mater. Struct. **24**, 063001 (2015).

[23] S. A. Emam and D. J. Inman, Appl. Mech. Rev. **67**, 060803 (2015).

[24] S. P. Pellegrini, N. Tolou, M. Schenk, and J. L. Herder, J. Intell. Mater. Syst. Struct. **24**, 1303 (2013).

[25] S. Saadon and O. Sidek, Energy Convers. Manage. **52**, 500 (2011).

[26] D. Zhu, M. J. Tudor, and S. P. Beeby, Meas. Sci. Technol. **21**, 022001 (2009).

[27] K. Bertoldi, V. Vitelli, J. Christensen, and M. van Hecke, Nat. Rev. Mater. **2**, 17066 (2017).

[28] S. Shan, S. H. Kang, J. R. Raney, P. Wang, L. Fang, F. Candido, J. A. Lewis, and K. Bertoldi, Adv. Mater. **27**, 4296 (2015).

[29] E. Blokhina, A. E. Aroudi, E. Alarcon, and D. Galayko, *Nonlinearity in Energy Harvesting Systems* (Springer, Berlin, 2016).

[30] W. A. Oldfather, C. A. Ellis, and D. M. Brown, Isis **20**, 72 (1933).

[31] A. E. H. Love, *A Treatise on the Mathematical Theory of Elasticity*, 4th ed., (Dover, New York, 1927).

[32] B. Roman and A. Pocheau, J. Mech. Phys. Solids **50**, 2379 (2002).

[33] B. Roman and A. Pocheau, Europhys. Lett. **46**, 602 (1999).

[34] A. R. Mojdehi, B. Tavakol, W. Royston, D. A. Dillard, and D. P. Holmes, Extreme Mech. Lett. **9**, 237 (2016).

[35] L. Stein-Montalvo, P. Costa, M. Pezzulla, and D. P. Holmes, Soft Matter **15**, 1215 (2019).

[36] D. J. Schunter, M. Brandenbourger, S. Perriseau, and D. P. Holmes, Phys. Rev. Lett. **120**, 078002 (2018).

[37] S. P. Timoshenko and J. M. Gere, *Theory of Elastic Stability*, 2nd ed. (McGraw-Hill, New York, 1961).

[38] A. Fargette, S. Neukirch, and A. Antkowiak, Phys. Rev. Lett. **112**, 137802 (2014).

[39] Y. Forterre, J. M. Skotheim, J. Dumais, and L. Mahadevan, Nature (London) **433**, 421 (2005).

[40] M. Gomez, D. E. Moulton, and D. Vella, Nat. Phys. **13**, 142 (2017).

[41] M. Gomez, D. E. Moulton, and D. Vella, J. Mech. Phys. Solids **124**, 781 (2019).

[42] M. Gomez, D. E. Moulton, and D. Vella, Phys. Rev. Lett. **119**, 144502 (2017).

[43] N. P. Bende, A. A. Evans, S. Innes-Gold, L. A. Marin, I. Cohen, R. C. Hayward, and C. D. Santangelo, Proc. Natl. Acad. Sci. **112**, 11175 (2015).

[44] E. Y. Urbach and E. Efrati, Sci. Adv. **6**, eabb2948 (2020).

[45] Y.-L. Pi and M. A. Bradford, Nonlinear Dyn. **73**, 1289 (2013).

[46] S. Jiao and M. Liu, ACS Appl. Mater. Interfaces **13**, 1158 (2021).

[47] J.-S. Chen and S.-Y. Hung, European Journal of Mechanics - A/Solids **30**, 525 (2011).

[48] A. Pandey, D. E. Moulton, D. Vella, and D. P. Holmes, Europhys. Lett. **105**, 24001 (2014).

[49] P. F. Byrd and M. D. Friedman, *Handbook of Elliptic Integrals for Engineers and Physicists*, 1st ed. (Springer, Berlin, 1954).

[50] A. J. Adams, J. Math. Phys. **49**, 032902 (2008).

[51] V. M. Vassilev, P. A. Djondjorov, and I. M. Mladenov, J. Phys. A: Math. Theor. **41**, 435201 (2008).

[52] S. V. Levyakov and V. V. Kuznetsov, Acta Mech. **211**, 73 (2010).

[53] M. Batista, Int. J. Solids Struct. **87**, 153 (2016).

[54] We note that the asymmetric-to-symmetric transition can be analyzed in several directions. While one direction is presented in the main text, another direction is to obtain the Landau expansion of the elastic energy [4]. To derive the latter expansion one needs, for example, to find a solution to the symmetric branch that yet does not satisfy Eq. (15a). Then substitute this solution

in $\bar{\mathcal{G}} = E - P_x[1 - \Delta - x(1)]$ and expand this energy in powers of the order parameter m^2. Of course, this direction and the one presented in the main text yields the same conclusions regarding the transition.

[55] The factor of 2 arises due to the fact the P_{ud} is conjugate to $\frac{1}{2}V_{\mathrm{du}}$ and not to V_{du}, see Eq. (4). In addition, the minus sign arises since $P_{\mathrm{ud}} = P_{\mathrm{u}} - P_{\mathrm{d}}$ measures the pressure drop between the upper and lower sides of the chamber, while $V_{\mathrm{du}} = V_{\mathrm{d}} - V_{\mathrm{u}}$ measures the volume difference in the opposite direction.

[56] W. R. Inc., Mathematica, Version 11.0, Champaign, IL, 2018.

[57] P. N. Nge, C. I. Rogers, and A. T. Woolley, Chem. Rev. **113**, 2550 (2013).

[58] S.-H. Chiu and C.-H. Liu, Lab Chip **9**, 1524 (2009).

[59] C.-Y. Lee, C.-L. Chang, Y.-N. Wang, and L.-M. Fu, Int. J. Mol. Sci. **12**, 3263 (2011).

[60] D. J. Preston, P. Rothemund, H. J. Jiang, M. P. Nemitz, J. Rawson, Z. Suo, and G. M. Whitesides, Proc. Natl. Acad. Sci. **116**, 7750 (2019).

[61] D. J. Preston, H. J. Jiang, V. Sanchez, P. Rothemund, J. Rawson, M. P. Nemitz, W.-K. Lee, Z. Suo, C. J. Walsh, and G. M. Whitesides, Science Robotics **4**, eaaw5496 (2019).

[62] G. Arena, R. M. J. Groh, A. Brinkmeyer, R. Theunissen, P. M. Weaver, and A. Pirrera, Proc. R. Soc. A **473**, 20170334 (2017).

[63] M. Di Ventra, Y. V. Pershin, and L. O. Chua, Proc. IEEE **97**, 1717 (2009).

[64] R. D. Yamaletdinov, O. V. Ivakhnenko, O. V. Sedelnikova, S. N. Shevchenko, and Y. V. Pershin, Sci. Rep. **8**, 3566 (2018).

[65] Note that when $u < 0$, i.e., P_x switches sign, we need to replace $u \rightarrow iu$ ($i = \sqrt{-1}$) in the corresponding equations.

[66] Y. L. Sachkov and S. V. Levyakov, Proceedings of the Steklov Institute of Mathematics **271**, 177 (2010).

[67] S. Krylov, B. R. Ilic, D. Schreiber, S. Seretensky, and H. Craighead, J. Micromech. Microeng. **18**, 055026 (2008).

[68] G. Arreaga, R. Capovilla, C. Chryssomalakos, and J. Guven, Phys. Rev. E **65**, 031801 (2002).

[69] I. M. Mladenov, P. A. Djondjorov, M. T. Hadzhilazova, and V. M. Vassilev, Commun. Theor. Phys. **59**, 213 (2013).

[70] I. Tadjbakhsh and F. Odeh, J. Math. Anal. Appl. **18**, 59 (1967).

[71] E. Katifori, S. Alben, and D. R. Nelson, Phys. Rev. E **79**, 056604 (2009).

[72] G. Valchev, P. Djondjorov, V. Vassilev, and D. Dantchev, J. Phys.: Condens. Matter **32**, 405001 (2020).

[73] R. Capovilla, C. Chryssomalakos, and J. Guven, Eur. Phys. J. B **29**, 163 (2002).

[74] V. Ferone, B. Kawohl, and C. Nitsch, Math. Ann. **365**, 987 (2016).

[75] M. Abramovitz and I. A. Stegun, *Handbook of Mathematical Functions*, 1st ed. (Dover, New York, 1972).